J. Fluid Mech. (2023), *vol*. 959, R1, doi:10.1017/jfm.2023.100

Linear stability analysis of purely elastic travelling-wave solutions in pressure-driven channel flows

Martin Lellep[1], Moritz Linkmann[2] and Alexander Morozov[1],†

[1]SUPA, School of Physics and Astronomy, The University of Edinburgh, James Clerk Maxwell Building, Peter Guthrie Tait Road, Edinburgh EH9 3FD, UK

[2]School of Mathematics and Maxwell Institute for Mathematical Sciences, The University of Edinburgh, Edinburgh EH9 3FD, UK

(Received 16 November 2022; revised 17 January 2023; accepted 29 January 2023)

Recent studies of pressure-driven flows of dilute polymer solutions in straight channels demonstrated the existence of two-dimensional coherent structures that are disconnected from the laminar state and appear through a subcritical bifurcation from infinity. These travelling-wave solutions were suggested to organise the phase-space dynamics of purely elastic and elasto-inertial chaotic channel flows. Here, we consider a wide range of parameters, covering the purely elastic and elasto-inertial cases, and demonstrate that the two-dimensional travelling-wave solutions are unstable when embedded in sufficiently wide three-dimensional domains. Our work demonstrates that studies of purely elastic and elasto-inertial turbulence in straight channels require three-dimensional simulations, and no reliable conclusions can be drawn from studying strictly two-dimensional channel flows.

Key words: polymers, shear-flow instability, bifurcation

1. Introduction

The past few years have seen a growing interest in understanding of pressure-driven channel flows of dilute polymer solutions (Castillo Sánchez *et al.* 2022; Datta *et al.* 2022). The state space of such flows is spanned by three dimensionless parameters: Re, the Reynolds number that measures the relative importance of inertia compared with viscous dissipation; Wi, the Weissenberg number that measures the strength of polymer-induced viscoelastic stresses; β, the solvent to the total solution viscosity ratio that is related to the polymer concentration. The rich variety of flow states associated with different

† Email address for correspondence: alexander.morozov@ed.ac.uk

parts of the (Re, Wi, β) space ranges from drag-reduction and elasto-inertial turbulence (Dubief, Terrapon & Hof 2023) to purely elastic instabilities and turbulence (Steinberg 2021), making it a subject of interest for turbulence and flow-control researchers, polymer rheologists and physicists studying flows of complex fluids (Castillo Sánchez *et al.* 2022; Datta *et al.* 2022).

The most significant recent advances in this area correspond to flows with small to negligible amounts of inertia. Such flows were believed to be laminar and exhibit no instabilities, until several studies challenged this view. While early results on pressure-driven channel flows of model dilute polymer solutions indicated their linear stability (Gorodtsov & Leonov 1967; Wilson, Renardy & Renardy 1999), Morozov & van Saarloos (2005, 2007, 2019) proposed a subcritical bifurcation from infinity as a nonlinear destabilisation mechanism, similar to Newtonian wall-bounded shear flows (Eckhardt 2018; Graham & Floryan 2021). The existence of such a subcritical bifurcation was demonstrated experimentally by Arratia and co-workers (Pan *et al.* 2013; Qin & Arratia 2017; Qin *et al.* 2019), while the more recent experiments by Steinberg and co-workers (Jha & Steinberg 2020, 2021; Shnapp & Steinberg 2022; Li & Steinberg 2022) provide insight into the spatial structure of the ensuing instability.

In addition to these developments, Shankar and co-workers re-visited the linear stability analysis of pressure-driven channel flows of model dilute polymer solutions, and identified a novel linear instability mechanism associated with the centre-line mode (Chaudhary *et al.* 2019; Khalid, Shankar & Subramanian 2021*b*; Khalid *et al.* 2021*a*). Although this linear instability exists in a narrow range of parameters, $1-\beta \ll 1$ and $Wi \gg 1$, which can be difficult to simultaneously realise experimentally, the nonlinear structures that stem from this instability appear to be crucial to the understanding of elasto-inertial and purely elastic channel flows. Page, Dubief & Kerswell (2020) and Buza, Page & Kerswell (2022) showed that for sufficiently large values of Re, the linear instability discussed above leads to a two-dimensional subcritical bifurcation that extends significantly outside of the (Re, Wi) region where the linear instability exists. Morozov (2022) performed direct numerical simulations of two-dimensional channel flow at negligible inertia, $Re \ll 1$, for a wide range of β and Wi, and reported the existence of purely elastic nonlinear travelling-wave solutions. These solutions, that we will refer to as the narwhals, appear through a bifurcation from infinity that ties their existence with the original proposal by Morozov & van Saarloos (2005, 2007, 2019). (Previous work referred to similar structures as arrowheads (Page *et al.* 2020; Buza *et al.* 2022; Dubief *et al.* 2022). We do not appreciate the association of that term with warfare, and, instead, prefer to call them narwhals, for the obvious likeness of their polymer stress distribution (see figure 1, for example). We are grateful to Professor Becca Thomases (Smith College) for suggesting the name.) Their obvious centre-mode character and their visual resemblance to the structures reported in the elasto-inertial regime (Page *et al.* 2020; Buza *et al.* 2022; Dubief *et al.* 2022) most likely imply that these structures belong to the same solution family that is ultimately connected to the centre-mode linear instability found in a rather special part of the (β, Wi, Re) parameter space.

While the narwhal solutions share many of the features observed in experiments (Pan *et al.* 2013; Qin & Arratia 2017; Qin *et al.* 2019; Jha & Steinberg 2020, 2021; Shnapp & Steinberg 2022; Li & Steinberg 2022), they do not represent chaotic flows; indeed, in two-dimensional channel flows, they are steady travelling-wave solutions. To be dynamically relevant, these structures are expected to lose their stability when embedded in three-dimensional domains, as is indeed the case with Newtonian Tollmien–Schlichting waves (Orszag & Patera 1983). The purpose of the current work is to study the

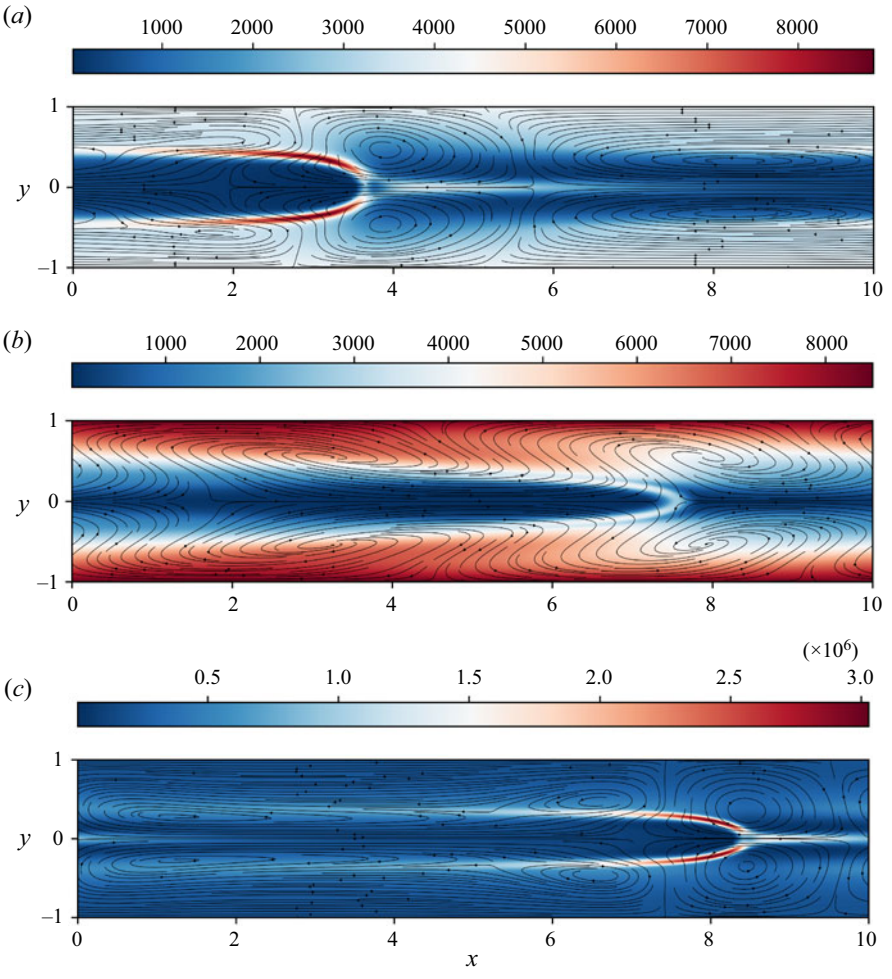

Figure 1. Examples of two-dimensional narwhal travelling-wave solutions used as the base state in our linear stability analysis. (*a*) A purely elastic state with $(Wi, \beta, Re) = (100, 0.8, 0.01)$ and $L_x = 10$, studied in Morozov (2022). (*b*) An elasto-inertial state with $(Wi, \beta, Re) = (45, 0.997, 90)$ and $L_x = 2\pi/2.18$, motivated by the work of Page *et al.* (2020). (*c*) A purely elastic state connected to the centre-mode instability found by Khalid *et al.* (2021*b*) with $(Wi, \beta, Re) = (1700, 0.997, 0.01)$ and $L_x = 2\pi/0.75$. The colours indicate values of tr($\boldsymbol{c}$) and solid lines show the streamlines of the velocity deviation from the streamwise-averaged flow profile. The mean flow is from left to right along the x-direction.

three-dimensional linear stability of the two-dimensional narwhal solutions discussed above. We report that in all cases studied here for a wide range of β, Wi and Re, the two-dimensional narwhal solutions lose their stability when embedded in a three-dimensional domain. We characterise this instability and discuss its implications for the mechanism of elastic and elasto-inertial turbulence.

2. Equations of motion and numerical details

We consider three-dimensional pressure-driven channel flow and select a Cartesian coordinate system with (x, y, z) being along the flow (streamwise), wall-normal and spanwise directions, correspondingly. The dimensionless equations of motion for the

polymeric fluid are given by the Phan-Thien–Tanner (PTT) constitutive model (Phan-Thien & Tanner 1977), coupled to the incompressible Navier–Stokes equation:

$$\partial_t \boldsymbol{c} + \boldsymbol{u}\cdot\nabla\boldsymbol{c} - \nabla\boldsymbol{u}^{\dagger}\cdot\boldsymbol{c} - \boldsymbol{c}\cdot\nabla\boldsymbol{u} = -\frac{\boldsymbol{c}-\boldsymbol{1}}{Wi}(1-3\epsilon+\epsilon\,\mathrm{tr}(\boldsymbol{c})) + \kappa\Delta\boldsymbol{c}, \tag{2.1}$$

$$\partial_t \boldsymbol{u} + \boldsymbol{u}\cdot\nabla\boldsymbol{u} = -\nabla p + \frac{\beta}{Re}\Delta\boldsymbol{u} + \frac{1-\beta}{ReWi}\nabla\cdot\boldsymbol{c} + \frac{2}{Re}\boldsymbol{e}_x, \tag{2.2}$$

$$\nabla\cdot\boldsymbol{u} = 0, \tag{2.3}$$

where the dagger denotes the transpose, $\boldsymbol{1}$ is the identity matrix, tr denotes the trace, $\boldsymbol{e}_x$ is the unit vector in the x-direction, $\boldsymbol{u}$ is the fluid velocity, $\boldsymbol{c}$ is the polymer conformation tensor and p is the pressure. The equations are rendered dimensionless by using d, $\mathcal{U}$, $d/\mathcal{U}$, $\eta_p\mathcal{U}/d$ and $(\eta_s+\eta_p)\mathcal{U}/d$ as the scales for length, velocity, time, stress and pressure, respectively. Here, d is the channel half-width, η_s and η_p are the solvent and polymeric contributions to the viscosity, and $\mathcal{U}$ is the centre-line value of the laminar fluid velocity of a Newtonian fluid with the viscosity $\eta_s+\eta_p$ at the same value of the applied pressure gradient. As discussed above, the state diagram of this flow is spanned by the viscosity ratio $\beta=\eta_s/(\eta_s+\eta_p)$, the Reynolds number $Re=\rho\mathcal{U}d/(\eta_s+\eta_p)$ and the Weissenberg number $Wi=\lambda\mathcal{U}/d$, where ρ is the density of the fluid and λ is the Maxwell relaxation time of polymer molecules. Finally, the constant ϵ controls the degree of shear-thinning of the model PTT fluid, and κ is a dimensionless polymer diffusivity. The stress-diffusion term in (2.1) is added to ensure that the conformation tensor $\boldsymbol{c}$ remains strictly positive-definite at all times throughout our work. We note that while some previous studies employed unrealistically large values of κ for this purpose, the value of κ used here is in line with the realistic values relevant to microfluidic experiments (Pan *et al.* 2013; Qin & Arratia 2017; Qin *et al.* 2019). See Morozov (2022) for the estimates of κ and its relationship to kinetic theories of dilute polymer solutions.

The starting point of our analysis are the narwhal travelling-wave solutions determined in Morozov (2022) by numerically advancing the two-dimensional version of (2.1)–(2.3) in time until a steady state was reached. We denote those states by $s_{2D}=\{\boldsymbol{u}_{2D}, p_{2D}, \boldsymbol{c}_{2D}\}(x-\phi_{2D}t, y)$, where ϕ_{2D} is the phase speed of the travelling wave. For each narwhal state, the corresponding value of ϕ_{2D} was determined numerically by tracking the spatial position of the largest value of $\mathrm{tr}(\boldsymbol{c}_{2D})$ as a function of time. In what follows, s_{2D} and ϕ_{2D} serve as the base state for our linear stability calculations.

To probe the linear stability of the two-dimensional narwhal states s_{2D} with respect to three-dimensional infinitesimal perturbations in the form $s_{3D}=\{\delta\boldsymbol{u}, \delta p, \delta\boldsymbol{c}\}(x-\phi_{2D}t, y, z, t)$, we linearise (2.1)–(2.3) in three dimensions around a two-dimensional travelling-wave state $s_{2D}=\{\boldsymbol{u}_{2D}, p_{2D}, \boldsymbol{c}_{2D}\}(x-\phi_{2D}t, y)$. The resulting linear equations for s_{3D} are stepped forward in time to determine the growth rate of the instability. The methodology employed here is similar to that used by Orszag & Patera (1983), who studied stability of Newtonian Tollmien–Schlichting waves. As the linearised equations of motion for s_{3D} decouple the time evolution of the Fourier modes in the z-direction, the full dispersion relation can be obtained from a single three-dimensional simulation. To this end, we introduce an observable $a(t, k_z)$ that is based on s_{3D} as follows:

$$a(t,k_z) = \left\langle \hat{\delta c}_{xx}(x-\phi_{2D}t, y, k_z, t)\hat{\delta c}^{*}_{xx}(x-\phi_{2D}t, y, k_z, t)\right\rangle_{x,y}. \tag{2.4}$$

Here, the hat denotes the Fourier transform along the z-direction, k_z is the wave number, and $\langle\cdots\rangle_{x,y}$ denote spatial average over the x- and y-directions. While $a(t, k_z)$ can, in

principle, be defined based on any component of s_{3D}, here we singled out δc_{xx} as it is the largest component of the conformation tensor and is the most dynamically active one. As we will see below, for sufficiently long times, $a(t, k_z) \sim e^{2\sigma(k_z)t}$, with $\sigma(k_z)$ being the real part of the leading eigenvalue. All eigenvalues reported in this work have zero imaginary parts up to numerical accuracy. Below, we refer to $\sigma = \sigma(k_z)$ as the dispersion relation.

Simulations are carried out using a parallel pseudo-spectral solver with full 3/2-dealiasing implemented in Dedalus (Burns *et al.* 2020) on a domain $[0, L_x] \times [-1, 1] \times [0, L_z]$, where L_x and L_z are the dimensionless system size in the streamwise and spanwise directions, respectively. We employ no-slip boundary conditions for the velocity, $\delta\boldsymbol{u}(x - \phi_{2D}t, y = \pm 1, z, t) = 0$, and natural boundary conditions for the conformational stress tensor, where $\delta\boldsymbol{c}(x - \phi_{2D}t, y = \pm 1, z, t)$ is set to the corresponding values of (2.1) with $\kappa = 0$ at each time step (Liu & Khomami 2013); periodic boundary conditions are used in the streamwise and spanwise directions. All fields are represented by Fourier decompositions in the periodic directions, and by a Chebyshev expansion in the y-direction using $N_x \times N_y \times N_z = 256 \times 1024 \times 128$ spectral modes. The time stepping uses a four-stage, third-order implicit-explicit Runge–Kutta method with the time step $dt = 5 \times 10^{-3}$. Each simulation is started from an s_{2D} narwhal state. To break its translational invariance in the z-direction, the perturbation component δc_{xx} is initialised with a Gaussian noise of zero mean and unit variance; the magnitude of the noise is selected to be 1×10^{-7} of the maximum value of the c_{xx} component of the narwhal conformation tensor.

3. Results

First, we analyse linear stability of the purely elastic narwhal solutions reported in Morozov (2022); see figure 1(*a*), for example. We set $L_x = L_z = 10$, $Re = 0.01$, $\epsilon = 10^{-3}$, $\kappa = 5 \times 10^{-5}$ and vary β and Wi. For these parameters, the laminar flow is linearly stable, and the two-dimensional travelling-wave solutions appear through a subcritical bifurcation from infinity. In what follows, the lowest value of Wi for each β considered here corresponds to the saddle-node of the subcritical bifurcation.

In figure 2(*a*), we present a typical evolution of the observable $a(t, k_z)$ for various values of k_z. As our initial condition comprises Gaussian noise, the initial projection on the most unstable eigenmode is small, and $a(t, k_z)$ initially decreases as a function of time. At sufficiently long times, the time evolution of $a(t, k_z)$ is dominated by the largest unstable eigenvalue that we determine by fitting an exponential $a(t, k_z) \sim e^{2\sigma(k_z)t}$ to its long-t behaviour, as discussed above. Examples of such fits are given by the dashed lines in figure 2(*a*). Combining $\sigma(k_z)$ as a function of k_z yields the dispersion relation for given β and Wi, and, in figure 2(*b*), we show several representative examples. All dispersion relations studied in this work have the same shape, and exhibit a peak in the $\sigma(k_z)$ curves, indicating an instability with a finite spanwise length scale. The largest growth rates and the corresponding values of k_z are presented in figure 3. We conclude that all two-dimensional narwhal solutions become linearly unstable when embedded in a three-dimensional domain.

To gain insight into the spatial structure of the instability, in figure 4 we plot the three-dimensional profile associated with the most unstable mode (the peak of $\sigma(k_z)$) for $\beta = 0.8$ and $Wi = 100$. For clarity, we only report a part of the simulation domain that contains a few instability periods in the spanwise direction, set by $k_{z,max}^{-1}$. As can be seen from figure 4(*a*,*c*), the polymer extension associated with the perturbation, $\mathrm{tr}(\delta\boldsymbol{c})$, is localised in thin sheets around the polymer extension of the base flow (the 'body' of the narwhal), with regions of polymer stretch and compression alternating along the spanwise direction. This stress distribution drives a periodic array

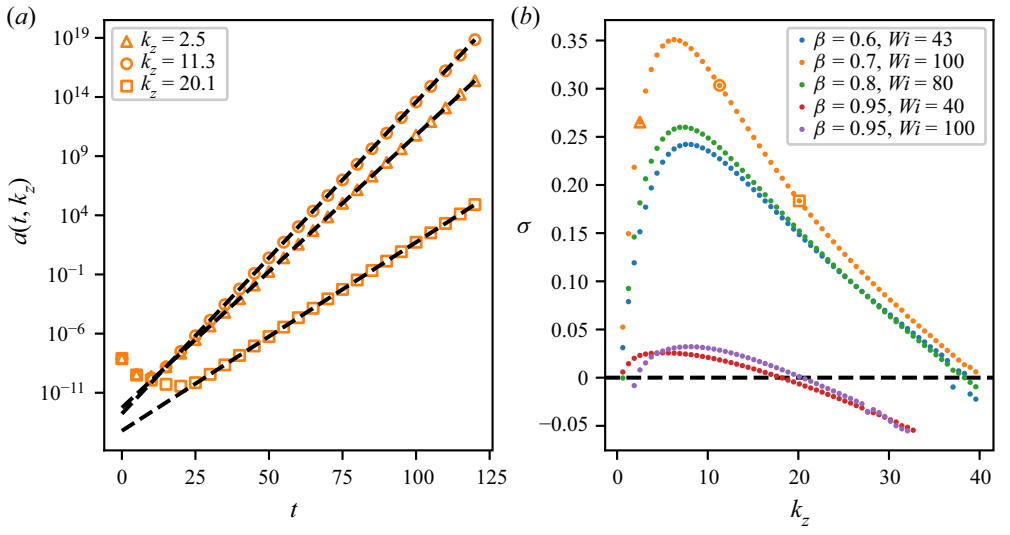

Figure 2. (*a*) Time evolution of the observable $a(t, k_z)$ defined in (2.4) for $(Wi, \beta) = (100, 0.7)$ and selected wave numbers. The black dashed lines show the exponential fits used to measure the growth rate $\sigma(k_z)$. (*b*) Dispersion relations for representative example values of (Wi, β). The symbols superposed on the $(Wi, \beta) = (100, 0.7)$ data (orange curve) represent the values of the growth rates determined from (*a*).

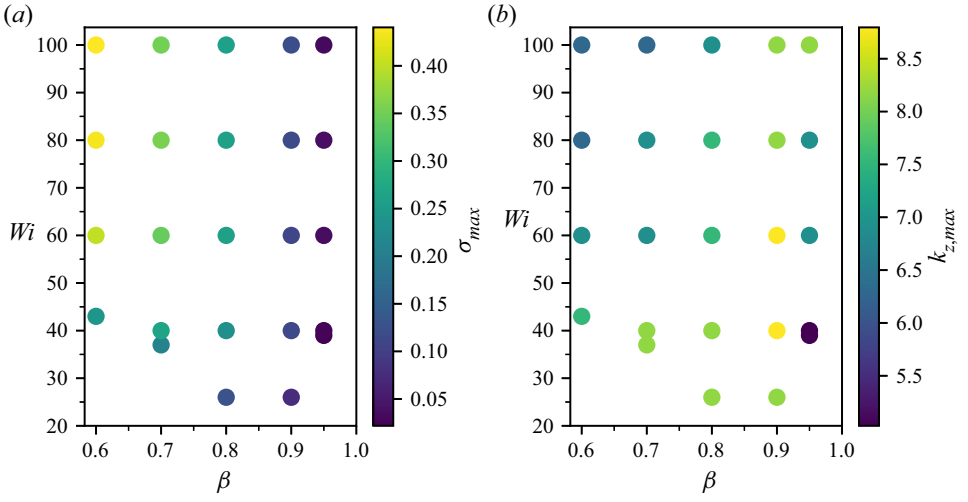

Figure 3. Results of linear stability analysis for the purely elastic narwhal solutions found in Morozov (2022). (*a*) The growth rates of the most unstable mode, $\sigma_{max} = \max_{k_z} \sigma(k_z)$, for various β and Wi. (*b*) The corresponding values of k_z that set the spanwise periodicity of the most unstable mode.

of vortices that are primarily confined to the streamwise-spanwise centre-plane, with the maxima/minima of the streamwise component of the velocity perturbation coinciding with the stretching/compression of the polymers.

Up to this point, our analysis was restricted to the case of the subcritical travelling-wave solutions that are disconnected from the laminar state. Next, we consider two sets of parameter values where the narwhal solutions are known to connect to a two-dimensional linear instability of the base state. The first corresponds to the purely elastic instability

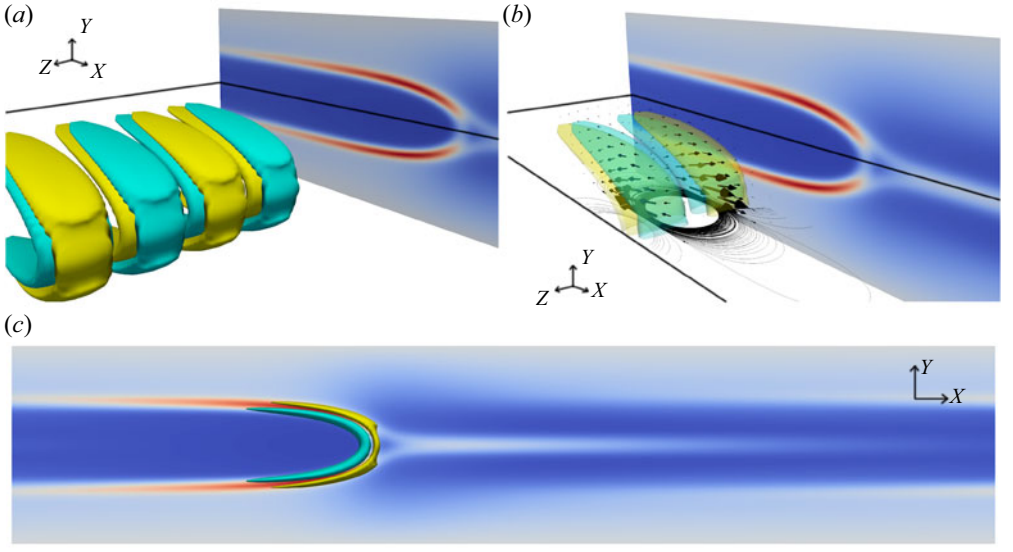

Figure 4. Representative example of the three-dimensional spatial profiles of the most unstable mode for $(Wi, \beta) = (100, 0.8)$ with $k_z \approx 6.91$. The two-dimensional base narwhal state is shown in the background of all subfigures, with the colour scheme indicating the magnitude of $\mathrm{tr}(\boldsymbol{c}_{2D})$. For visualisation purposes we show either one or two periods of the perturbation in the spanwise direction only. (*a*) Isosurfaces of the perturbation $\mathrm{tr}(\delta\boldsymbol{c})$, with light/dark colour showing polymer extension/compression. The same structures are shown in (*b*) alongside the perturbation velocity field, shown by the arrows, and the centre-plane streamfunction, shown by the solid lines. (*c*) Planar view of the base state and a half-period of the perturbation that demonstrates that the perturbation stresses are localised on both sides of the narwhal 'body', as discussed in the main text.

identified for $1 - \beta \ll 1$ and $Wi \ll 1$ by Khalid *et al.* (2021*b*). To match the parameters of the linear instability identified in that work, we set $L_x = 2\pi/0.75$, $L_z = 10$, $Re = 0.01$, $Wi = 1700$ and $\beta = 0.997$. To demonstrate that the three-dimensional instability reported here also exists in the elasto-inertial regime, we consider the following set of parameters motivated by the work of Page *et al.* (2020): $L_x = 2\pi/2.18$, $L_z = 10$, $Re = 90$, $Wi = 45$ and $\beta = 0.9$. In both cases we set $\epsilon = 5 \times 10^{-5}$ and $\kappa = 3 \times 10^{-5}$.

For these two sets of parameters, we performed two-dimensional direct numerical simulations, similar to Morozov (2022), and obtained steady travelling-wave solutions, shown in figure 1. Note that our elasto-inertial narwhal solution differs slightly from that obtained by Page *et al.* (2020), as those authors considered constant-flux channel flow, while we study the constant-pressure-gradient case. In figure 5, we present the dispersion relation of the three-dimensional linear stability analysis for these two sets of parameters. Although the high-Wi, high-β case associated with the centre-mode instability in two dimensions leads to a significantly weaker three-dimensional instability, yet again, both two-dimensional structures are linearly unstable when embedded in three-dimensional domains.

4. Discussion

Recent numerical studies of pressure-driven channel flows of dilute polymer solutions identified narwhal travelling-wave solutions as steady coherent structures dominating purely elastic (Buza *et al.* 2022; Morozov 2022) and elasto-inertial (Page *et al.* 2020; Dubief *et al.* 2022) two-dimensional flows. In this work, we analysed linear stability of these two-dimensional structures upon their embedding in three-dimensional domains.

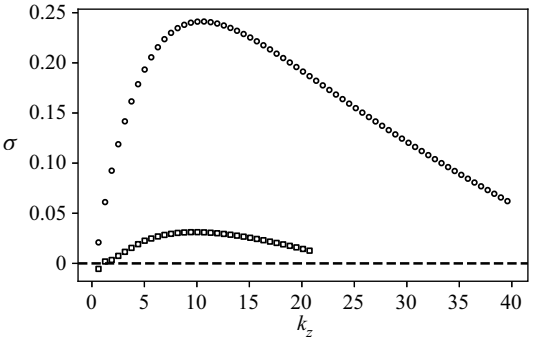

Figure 5. Dispersion relations for $(Wi, \beta, Re) = (1700, 0.997, 0.01)$ and $(L_x, L_z) = (2\pi/0.75, 10)$ (open squares), and $(Wi, \beta, Re) = (45, 0.9, 90)$ and $(L_x, L_z) = (2\pi/2.18, 10)$ (open circles).

In all parts of the parameter space (Re, Wi, β) studied here, both purely elastic and elasto-inertial, we find that the narwhal solutions become linearly unstable to perturbations periodic in the spanwise direction. The structure of the unstable mode and the shape of the dispersion relation are reminiscent of the linear instability reported in the literature in viscoelastic flows with strong spatial gradients of the polymer normal stress (Renardy 1988; Hinch *et al.* 1992) and in shear-banded flows (Fielding & Wilson 2010; Nicolas & Morozov 2012). Here, the role of the surface of large polymer extension is played by the thin sheets of high polymer stress constituting the body of the narwhal solution, as can be seen from figure 1. This observation is supported by figure 4(*c*) that shows that the polymer stretch associated with the three-dimensional perturbation is confined to a narrow vicinity of the high-stress region of the narwhal base state. While the instability exists for a wide range of the wave numbers k_z, the length scale associated with the most unstable mode, figure 3(*b*), is commensurate with the extent of the narwhal body in the wall-normal direction. As can also be seen from figure 3(*a*), the instability time scale is sufficiently short to result in a quick transition away from the base two-dimensional state.

Stability properties of the narwhal solutions reported above mirror closely the behaviour of Tollmien–Schlichting travelling-wave solutions in Newtonian pressure-driven channel flows. There, stable two-dimensional Tollmien–Schlichting waves appear through a linear instability at $Re = 5772$ in sufficiently long domains (Orszag 1971), and extend subcritically to significantly lower values of Re (Herbert 1976). Infinitesimal three-dimensional perturbations are, however, sufficient to drive the flow away from the two-dimensional structures, leading directly towards the turbulent state (Orszag & Patera 1983). The analogy with the Tollmien–Schlichting waves has significant implications for our understanding of turbulent dynamics in the presence of polymers. Since the narwhal solutions are unstable in three dimensions, they can be seen as an effective route to ignite purely elastic or elasto-intertial turbulence. However, similar to Tollmien–Schlichting waves in the Newtonian case, narwhal solutions are unlikely to be dynamically relevant in three dimensions. There are two reasons for this. Firstly, the solutions are low-dimensional and will therefore only occupy a small region in the high-dimensional phase space of a three-dimensional chaotic flow. Secondly, as we show here, narwhal solutions are unstable to perturbations at many length scales, hence any phase-space trajectory is unlikely to spend sufficiently long time in their vicinity. While recent studies suggested that elasto-inertial turbulence could be quasi-two-dimensional in nature (Dubief, Terrapon & Soria 2013; Samanta *et al.* 2013; Sid, Terrapon & Dubief 2018; Shekar *et al.* 2019, 2021), our results demonstrate that no conclusions about purely elastic or elasto-inertial flows can

be drawn from studying strictly two-dimensional versions of such flows; their properties can only be accessed by three-dimensional simulations.

Acknowledgements. We gratefully acknowledge the support we received from the Dedalus team (https://dedalus-project.org), and Keaton Burns in particular.

Funding. Computational resources on ARCHER2 (www.archer2.ac.uk) were provided by the UK Turbulence Consortium (https://www.ukturbulence.co.uk/, EPSRC grant number EP/R029326/1). We acknowledge financial support from the German Academic Scholarship Foundation (Studienstiftung des deutschen Volkes) and this work received funding from Priority Programme SPP 1881 'Turbulent Superstructures' of the Deutsche Forschungsgemeinschaft (DFG, grant number Li3694/1). For the purpose of open access, the authors have applied a Creative Commons Attribution (CC BY) licence to any Author Accepted Manuscript version arising from this submission.

Declaration of interests. The authors report no conflict of interest.

Author ORCIDs.
Martin Lellep https://orcid.org/0000-0003-1802-6973;
Moritz Linkmann https://orcid.org/0000-0002-3394-1443;
Alexander Morozov https://orcid.org/0000-0003-4498-3910.

References

Burns, K.J., Vasil, G.M., Oishi, J.S., Lecoanet, D. & Brown, B.P. 2020 Dedalus: a flexible framework for numerical simulations with spectral methods. *Phys. Rev. Res.* **2**, 023068.

Buza, G., Page, J. & Kerswell, R.R. 2022 Weakly nonlinear analysis of the viscoelastic instability in channel flow for finite and vanishing Reynolds numbers. *J. Fluid Mech.* **940**, A11.

Castillo Sánchez, H.A., Jovanović, M.R., Kumar, S., Morozov, A., Shankar, V., Subramanian, G. & Wilson, H.J. 2022 Understanding viscoelastic flow instabilities: Oldroyd-b and beyond. *J. Non-Newtonian Fluid Mech.* **302**, 104742.

Chaudhary, I., Garg, P., Shankar, V. & Subramanian, G. 2019 Elasto-inertial wall mode instabilities in viscoelastic plane Poiseuille flow. *J. Fluid Mech.* **881**, 119–163.

Datta, S.S., *et al.* 2022 Perspectives on viscoelastic flow instabilities and elastic turbulence. *Phys. Rev. Fluids* **7**, 080701.

Dubief, Y., Page, J., Kerswell, R.R., Terrapon, V.E. & Steinberg, V. 2022 First coherent structure in elasto-inertial turbulence. *Phys. Rev. Fluids* **7**, 073301.

Dubief, Y., Terrapon, V.E. & Hof, B. 2023 Elasto-inertial turbulence. *Annu. Rev. Fluid Mech.* **55** (1), 675–705.

Dubief, Y., Terrapon, V.E. & Soria, J. 2013 On the mechanism of elasto-inertial turbulence. *Phys. Fluids* **25** (11), 110817.

Eckhardt, B. 2018 Transition to turbulence in shear flows. *Physica* A **504**, 121–129.

Fielding, S.M. & Wilson, H.J. 2010 Shear banding and interfacial instability in planar Poiseuille flow. *J. Non-Newtonian Fluid Mech.* **165**, 196–202.

Gorodtsov, V.A. & Leonov, A.I. 1967 On a linear instability of a plane parallel Couette flow of viscoelastic fluid. *Z. Angew. Math. Mech.* **31**, 310–319.

Graham, M.D. & Floryan, D. 2021 Exact coherent states and the nonlinear dynamics of wall-bounded turbulent flows. *Annu. Rev. Fluid Mech.* **53** (1), 227–253.

Herbert, T. 1976 Periodic secondary motions in a plane channel. In *Proceedings of the Fifth International Conference on Numerical Methods in Fluid Dynamics, June 28-July 3, 1976, Twente University of Technology* (ed. A.I. van de Vooren & P.J. Zandbergen). Springer.

Hinch, E.J., *et al.* 1992 The instability mechanism for two elastic liquids being co-extruded. *J. Non-Newtonian Fluid Mech.* **43**, 311–324.

Jha, N.K. & Steinberg, V. 2020 Universal coherent structures of elastic turbulence in straight channel with viscoelastic fluid flow. arXiv:2009.12258.

Jha, N.K. & Steinberg, V. 2021 Elastically driven Kelvin–Helmholtz-like instability in straight channel flow. *Proc. Natl Acad. Sci. USA* **118** (34), e2105211118.

Khalid, M., Chaudhary, I., Garg, P., Shankar, V. & Subramanian, G. 2021*a* The centre-mode instability of viscoelastic plane Poiseuille flow. *J. Fluid Mech.* **915**, A43.

KHALID, M., SHANKAR, V. & SUBRAMANIAN, G. 2021*b* Continuous pathway between the elasto-inertial and elastic turbulent states in viscoelastic channel flow. *Phys. Rev. Lett.* **127**, 134502.

LI, Y. & STEINBERG, V. 2022 Elastic instability in a straight channel of viscoelastic flow without prearranged perturbations. https://arxiv.org/abs/2201.06342.

LIU, N. & KHOMAMI, B. 2013 Elastically induced turbulence in Taylor–Couette flow: direct numerical simulation and mechanistic insight. *J. Fluid Mech.* **737**, R4.

MOROZOV, A. 2022 Coherent structures in plane channel flow of dilute polymer solutions with vanishing inertia. *Phys. Rev. Lett.* **129**, 017801.

MOROZOV, A.N. & VAN SAARLOOS, W. 2005 Subcritical finite-amplitude solutions for plane Couette flow of viscoelastic fluids. *Phys. Rev. Lett.* **95**, 024501.

MOROZOV, A.N. & VAN SAARLOOS, W. 2007 An introductory essay on subcritical instabilities and the transition to turbulence in visco-elastic parallel shear flows. *Phys. Rep.* **447**, 112–143.

MOROZOV, A. & VAN SAARLOOS, W. 2019 Subcritical instabilities in plane Poiseuille flow of an Oldroyd-B fluid. *J. Stat. Phys.* **175**, 554–577.

NICOLAS, A. & MOROZOV, A. 2012 Nonaxisymmetric instability of shear-banded Taylor–Couette flow. *Phys. Rev. Lett.* **108**, 088302.

ORSZAG, S.A. 1971 Accurate solution of the Orr–Sommerfeld stability equation. *J. Fluid Mech.* **50**, 689–703.

ORSZAG, S.A. & PATERA, A.T. 1983 Secondary instability of wall-bounded shear flows. *J. Fluid Mech.* **128**, 347–385.

PAGE, J., DUBIEF, Y. & KERSWELL, R.R. 2020 Exact traveling wave solutions in viscoelastic channel flow. *Phys. Rev. Lett.* **125**, 154501.

PAN, L., MOROZOV, A., WAGNER, C. & ARRATIA, P.E. 2013 Nonlinear elastic instability in channel flows at low Reynolds numbers. *Phys. Rev. Lett.* **110**, 174502.

PHAN-THIEN, N. & TANNER, R.I. 1977 A new constitutive equation derived from network theory. *J. Non-Newtonian Fluid Mech.* **2**, 353–365.

QIN, B. & ARRATIA, P.E. 2017 Characterizing elastic turbulence in channel flows at low Reynolds number. *Phys. Rev. Fluids* **2**, 083302.

QIN, B., SALIPANTE, P.F., HUDSON, S.D. & ARRATIA, P.E. 2019 Flow resistance and structures in viscoelastic channel flows at low Re. *Phys. Rev. Lett.* **123**, 194501.

RENARDY, Y. 1988 Stability of the interface in two-layer Couette flow of upper convected Maxwell liquids. *J. Non-Newtonian Fluid Mech.* **28**, 99–115.

SAMANTA, D., DUBIEF, Y., HOLZNER, M., SCHÄFER, C., MOROZOV, A.N., WAGNER, C. & HOF, B. 2013 Elasto-inertial turbulence. *Proc. Natl Acad. Sci. USA* **110** (26), 10557–10562.

SHEKAR, A., MCMULLEN, R.M., MCKEON, B.J. & GRAHAM, M.D. 2021 Tollmien–Schlichting route to elastoinertial turbulence in channel flow. *Phys. Rev. Fluids* **6**, 093301.

SHEKAR, A., MCMULLEN, R.M., WANG, S.-N., MCKEON, B.J. & GRAHAM, M.D. 2019 Critical-layer structures and mechanisms in elastoinertial turbulence. *Phys. Rev. Lett.* **122**, 124503.

SHNAPP, R. & STEINBERG, V. 2022 Non-modal elastic instability and elastic waves in weakly perturbed channel flow. *Phys. Rev. Fluids* **7**, 063901.

SID, S., TERRAPON, V.E. & DUBIEF, Y. 2018 Two-dimensional dynamics of elasto-inertial turbulence and its role in polymer drag reduction. *Phys. Rev. Fluids* **3**, 011301.

STEINBERG, V. 2021 Elastic turbulence: an experimental view on inertialess random flow. *Annu. Rev. Fluid Mech.* **53**, 27–58.

WILSON, H.J., RENARDY, M. & RENARDY, Y. 1999 Structure of the spectrum in zero Reynolds number shear flow of the UCM and Oldroyd-B liquids. *J. Non-Newtonian Fluid Mech.* **80**, 251–268.